# Correlation between filament deposition path, microstructural and mechanical properties of dense alumina parts printed by robocasting

Delphine Gourdonnaud, Vincent Pateloup, Anna Junger, Julie Bourret, Thierry Chartier, Pierre-Marie Geffroy

# *Correlation between filament deposition path, microstructural and mechanical properties of dense alumina parts printed by robocasting*

Delphine Gourdonnaud [a,*], Vincent Pateloup [a], Anna Junger [b], Julie Bourret [a], Thierry Chartier [a], Pierre-Marie Geffroy [a]

[a] *CNRS, Institute of Research for Ceramics (IRCER), UMR 7315, University of Limoges, European Ceramics Center, 12 rue Atlantis, F-87068 Limoges Cedex, France*

[b] *Wrocław University of Science and Technology, 50-370 Wrocław, Poland*

** Corresponding author. Tel.: +33 (0)587502344*
*Email address: delphine.gourdonnaud@unilim.fr (D. Gourdonnaud).*

## Abstract

Robocasting is an extrusion-based additive manufacturing (AM) process widely used to produce porous structures. It enables to build three-dimensional (3D) ceramic parts, thanks to computer numerical control of the filament deposition path onto a fabrication substrate. Despite its high potential, robocasting is much less explored than other AM techniques for producing dense parts.

This work focused on the robocasting of dense alumina parts by varying the filament deposition path. Taguchi method was used to establish a correlation between the printing parameters and the microstructural and mechanical properties of the sintered parts. Closed pores located between adjacent filaments were found to dictate crack propagation mechanisms, depending on the infill pattern. The optimal printing strategy led to 93% dense alumina samples having a flexural strength of 140 MPa, a Young's modulus of 355 GPa and a Poisson's ratio of 0.23.

## Keywords

Printing parameters; Additive manufacturing; Porosity; Young's modulus; Flexural strength

## 1. Introduction

The robocasting process, also known as direct ink writing (DIW), was initially developed in 1997 in Sandia laboratories by Cesarano *et al.* [1,2]. This process is an extrusion-based additive manufacturing technique which makes it possible the production of 3D ceramic parts with complex shapes. Robocasting is based on the forced flow of a paste through a nozzle with an internal diameter in the sub-millimeter range [1,3]. 3D parts are built using the automated nozzle position control. A slicer software calculates the toolpath from a computer-assisted design (CAD) model, then outputs it to G-code data. Extruded filaments are therefore deposited onto a substrate in a layer-by-layer approach, with an appropriate infill pattern (*i.e.* printing strategy) for each slice of the CAD model [4,5].

Despite a fairly simple principle, robocasting involves several requirements and process conditions that are likely to influence the final properties of the printed parts. For instance, regarding rheology, a shear-thinning behaviour (with a yield stress) is required to allow paste flowability during extrusion, and then to ensure excellent shape retention of the green body after deposition [6,7]. Lamnini *et al.* [8] reported a non-exhaustive list of variables influencing the outcome of robocasting. These are classified according to three main stages of the manufacturing process, namely: (i) paste formulation and properties (*e.g.* solid loading, viscosity, yield stress, drying kinetics), (ii) robocasting conditions (*e.g.* manufacturing environment, printing substrate, nozzle and plunger material and shape, nozzle diameter, barrel pressure, printing speed, filament deposition path, etc.) and (iii) post-processing (*e.g.* drying step, debinding and sintering schedules).

In the field of ceramics, there are known protocols to study and optimize both the paste formulation and the post-processing stages. However, little has been reported on the influence of robocasting conditions – particularly the filament deposition path – on the resulting properties of printed parts such as density, shrinkage, surface roughness or mechanical properties [8]. Classically, literature works rely either on previous studies or on empirical approaches to optimize printing strategies. However, no direct correlation has been established yet between printing parameters and the final performance of a printed part, let alone an explanation regarding the evolution of one in relation to the other.

Although robocasting is clearly established for the production of porous lattice structures for various applications [9–11], its use to build dense objects is much less reported. As an example, only few studies [5,12,13] have investigated the influence of the tool path used to create the printing orientations of dense specimens in the shape of a bar (lengthwise, width wise or a combination of both). In the case of such simple infill patterns, the most fragile layers (*i.e.* those printed width wise) seem to dictate the strength of materials, as shown in Table 1. However, it should be noted that comparing the results of different studies (Table 1) might be challenging due to variations in ceramic formulations and/or in testing methods. For instance, three-point bending tends to yield more optimistic flexural strength values compared to four-point bending, the latter distributing the load more evenly along the specimen. The outcome of mechanical tests is also strongly related to surface finishing (samples are sometimes polished up to 1 µm [5]), printing resolution, filament layer-to-layer alignment, and inter-filament porosity [14].

Table 1. Non-exhaustive list of data reported in the literature, regarding the influence of the infill pattern on the final properties of alumina parts printed by robocasting.

| Filament orientation | Ink or paste solid loading (vol%) | Relative density (%) | Flexural strength $\sigma_f$ (MPa) * | Young's modulus $E$ (GPa) | Ref. |
|---|---|---|---|---|---|
| **Lengthwise** | 38 | 97 | 297 (4P) (HL) | - | [5] |
| | 60 | 94 | 306 (4P) (AL) | - | [12] |

| | | | | | |
|---|---|---|---|---|---|
| | 50 | 97 | 280 (3P) (AL) | 350 | [13] |
| | 50 | 98 | 340 (3P) (AL) | 350 | [13] |
| **Width wise** | 38 | 97 | 265 (4P) (HL) | - | [5] |
| | 60 | 94 | 238 (4P) (AL) | - | [12] |
| | 50 | 95 | 170 (3P) (AL) | 290 | [13] |
| **Hatched 90°** | 60 | 94 | 241 (4P) (AL) | - | [12] |
| | 50 | 97 | 180 (3P) (AL) | 325 | [13] |
| **Other** | 38 | 97 | 220 (4P) (HL) | - | [5] |
| | 38 | 91 | 350 (4P) (HL) | - | [15] |
| | 42 | 85 | 100-300 (4P) (HL) | - | [15] |
| | 53 - 56 | 98 | 134-157 (3P) | - | [16] |

* (3P) three-point bending tests; (4P) four-point bending tests; (AL) aligned layup of filaments; (HL) hexagonal layup of filaments.

In the current state of knowledge, there is no information on the impact of more complex infill patterns. Serdeczny *et al.* [17] yet reported the significant influence of printing parameters for the mesostructure, or macroporosity, in 3D-printed materials. By varying simultaneously, the crushing, overlapping and layer-to-layer alignment of the extruded filaments, a change in the size and shape of the closed pores located between two adjacent filaments, as well as in bond line density, was observed. However, all of this is likely to impact crack propagation mechanisms, thus the mechanical properties of 3D-printed parts.

The present work aims to determine the influence of complex infill patterns on the microstructural and mechanical properties of the dense parts printed by robocasting. In addition to addressing a crucial aspect of the robocasting process, this study was conducted in an innovative manner using an eco-friendly ceramic paste, entirely composed of natural-origin additives, in order to meet the environmental challenges of our time. After a preliminary optimization of the other stages of the manufacturing process, alumina bending test parts have been produced under the same conditions, by only varying the nozzle deposition path. A particular attention was paid to four printing parameters, using the Taguchi method: (i) hatching angle from one layer to another, (ii) layer thickness, (iii) number of lines around the infill pattern and (iv) centre-to-centre distance between two adjacent filaments of the same layer (see Fig. 2). Grain size, shrinkage, relative density, closed porosity, flexural strength and elastic properties of sintered alumina samples were characterized and compared to the reported values of alumina. Taguchi design analysis allowed to define the influence and optimal conditions of the filament deposition path, in order to maximise the mechanical properties of robocast parts.

## 2. Experimental

### *2.1. Paste formulation*

An aqueous suspension of alumina powder (P172SB, Alteo, France), with an average particle size of 0.4 µm and a specific surface area of 7.3 $m^2.g^{-1}$ (BET method), was initially prepared by mixing it with 1 wt% (based on alumina solid content) of ammonium lignosulfonate (STARLIG AM®, LignoStar Group B.V., The Netherlands) in deionized water. The suspension

was homogenised in a planetary ball mill, then dried in an oven until the free water is completely removed. The resulting dried compact was then crushed and sieved through a mesh of 200 µm to obtain a pre-dispersed alumina powder, free of large agglomerates. Granulometric analyses revealed that the pre-dispersed powder exhibited a particle size distribution similar to that of the initial alumina powder, with a $D_{90}$ of 0.97 µm (1.05 µm for the initial powder).

A 49 vol% alumina paste was then prepared by adding 1.1 wt% of binder and 3.9 wt% of plasticizer relative to the mass of the pre-dispersed powder. A guar gum gel (G4129, Sigma-Aldrich Chimie SARL, France) was used as a binder and glycerol (Alfa Aesar A16205, Thermo Fisher GmbH, Germany) as a plasticizer. The latter is widely used in ceramic formulations, due to its low molecular weight, hygroscopic nature, and lubricating properties [18,19]. All these components were mixed in a THINKY ARE-250 machine at 1,000 rpm for 3 min.

An in-depth characterization of the rheological properties of the as-prepared alumina paste is reported in a previous work [20]. Its viscoelastic behaviour of was studied using a Discovery HR-2 Rheometer (TA Instruments) in oscillatory mode. Dynamic analyses with amplitude sweep were performed at 1 Hz, using a 4 mm diameter parallel plate with a 2,000 µm gap size. Results are presented in Fig. 1.a. In the linear viscoelastic region (LVER), the storage ($G'$) and loss ($G''$) moduli are $1\times10^8$ and $2\times10^7$ Pa, respectively. These values exceed those typically reported in the literature [15], mostly using inks (more fluid) rather than pastes. In contrast to inks, the higher the storage modulus $G'$, the greater the stiffness and resistance to reversible deformation of the paste, allowing for the printing of higher parts without the risk of collapse.

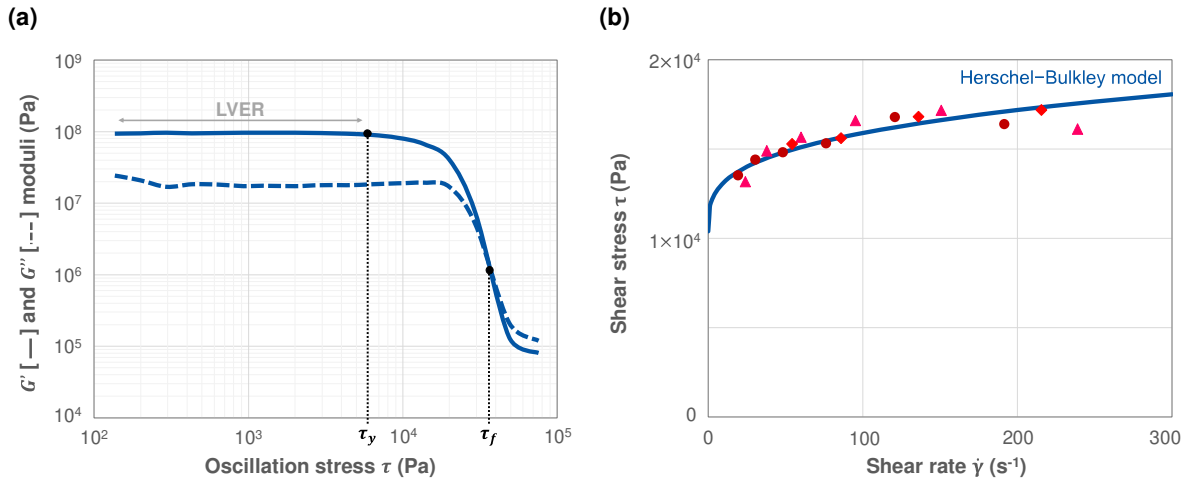


Fig. 1. Rheological characterizations performed on the as-prepared eco-friendly alumina paste: (a) Oscillatory amplitude sweep test. (b) Shear stress vs. shear rate described by the Herschel-Bulkley model (blue line); data were obtained from a capillary rheometry assembly installed on the extrusion head, using three different capillary ratios, of 8.36, 10.61 and 18.64 (red marks)

In addition, the paste shear-thinning behaviour was highlighted through capillary rheometry tests and described with the Herschel-Bulkley model, as shown in Fig. 1.b, after having applied

the Bagley's, Weißenberg-Rabinowitsch's and Mooney's corrections. The Herschel-Bulkley model [21] describes pasty fluids such as:

$$\tau = \tau_s + k \times \dot{\gamma}^n \quad (1)$$

where $\tau_s$ is the yield shear stress, $k$ is the consistency index and $n$ is the flow behaviour index.

The Herschel-Bulkley model allowed to identify the flow properties of the alumina paste used in this work: $\tau_s$ equals 103,876 Pa and $k$ is 13,714 Pa.s$^n$, with $n$ = 0.3. According to Fig. 1.b, this paste flows at a viscosity (or shear stress) close to its minimum (or maximum) value when sheared at least at 160 s$^{-1}$. Preliminary printability tests performed under this shear rate showed a good flow of the paste with excellent shape retention after deposition of the filaments.

*2.2. Printing of patterned alumina samples*

An in-house designed robocasting machine was used to print prismatic alumina bending test parts of a rectangular cross section (green parts of 62×7×6 mm$^3$). It consists of an extrusion head mounted on a computer numerical control (CNC) machine to build 3D parts in a layer-by-layer procedure. The as-prepared alumina paste was loaded as feedstock material into a 20 mm inner diameter barrel. It was extruded through a nozzle with an internal diameter of 1 mm, which corresponds to a good compromise between printing resolution and manufacturing time for this study. Printing speed was set at 20 mm.s$^{-1}$, corresponding to a shear rate of 160 s$^{-1}$. An upstream study [20] allowed to optimize some printing conditions, such as the substrate on which samples were printed (masking tape) and the manufacturing environment (20-22 °C, 65-75% of relative humidity).

A script in python language was used as a slicer in order to calculate the filament deposition paths from a CAD model and to generate it in G-code. Compared to conventional slicers, this method allows an adapted control of both the printing parameters and the deposition path geometry for the robocasting of ceramic pastes.

A particular attention was paid to four printing parameters: (i) the hatching angle from one layer to another, (ii) the layer thickness, (iii) the number of lines around the infill pattern and (iv) the hatching distance between two adjacent filaments of the same layer. The latter are shown within a bending test sample in Fig. 2.

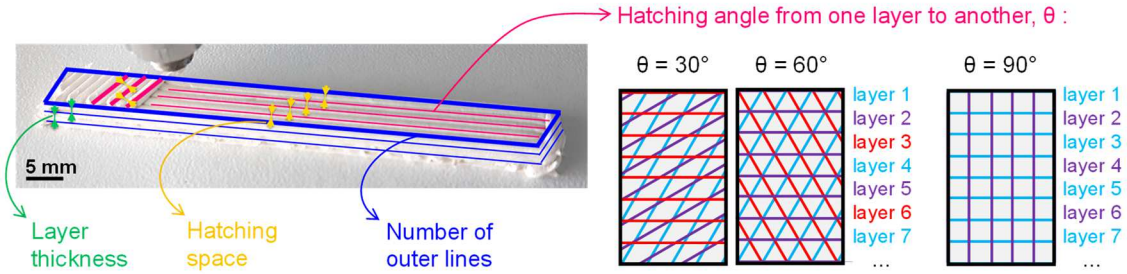


Fig. 2. Schematic representation of the four-studied parameters likely to influence the properties of alumina bending test parts printed by robocasting, due to a different infill pattern.

Varying the orientation (hatching angle θ = 30, 60 and 90°), the crushing (layer thickness $h$ = 0.5, 0.7 and 0.9 mm) and the spacing of the filaments (hatching space $d$ = 1.0, 1.1 and 1.2 mm) inside the infill pattern, as well as the number of outer lines (0, 1, 2), allowed to study to what extent the filament deposition path may affect the final properties of alumina bending test parts. This led to a four-factor design of experiment (DOE) varying on three levels. The latter, described in Table 2, consists of nine printing programs defined by the Taguchi method.

Table 2. Description of the DOE used to study the influence of the filament deposition path on the properties of robocast alumina parts.

| Samples | Hatching angle θ (°) | Layer thickness $h$ (mm) | Number of outer lines | Hatching space $d$ (mm) | Parameter $o\mathcal{F}$ (%) |
|---|---|---|---|---|---|
| **E01** | 30 | 0.5 | 0 | 1.0 | 62 |
| **E02** | 30 | 0.7 | 1 | 1.1 | 95 |
| **E03** | 30 | 0.9 | 2 | 1.2 | 132 |
| **E04** | 60 | 0.5 | 1 | 1.2 | 75 |
| **E05** | 60 | 0.7 | 2 | 1.0 | 86 |
| **E06** | 60 | 0.9 | 0 | 1.1 | 121 |
| **E07** | 90 | 0.5 | 2 | 1.1 | 68 |
| **E08** | 90 | 0.7 | 0 | 1.2 | 104 |
| **E09** | 90 | 0.9 | 1 | 1.0 | 109 |

In Table 2, a fifth parameter was adjusted for each experiment, namely overflow ($o\mathcal{F}$). The overflow is a function of the nozzle diameter ($n$ = 1 mm), the hatching space $d$ and the layer thickness $h$, as shown in Eq. 2. In the script generating G-codes, $o\mathcal{F}$ acts as a constant corrective parameter of the extruded flow, so as to fill the entire swept volume of a dense part and achieve a theoretical relative filling of 100%, as shown in Fig. 3.

$$o\mathcal{F} = \frac{1}{n^2}\left[\frac{2dh}{\pi} + \frac{h^2}{4} + \frac{2h}{\pi}\left(d - \frac{h}{2}\right)\right] \quad (2)$$

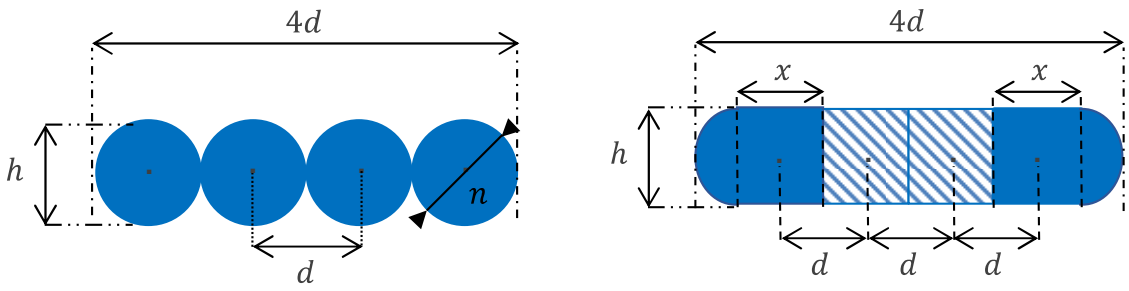


Fig. 3. Schematic representation of the action of the overflow parameter ($o\mathcal{F}$) on the extruded material (cross-sectional view of four deposited filaments), the other printing parameters remaining constant.

Fig. 4 shows green alumina bending test parts corresponding to each experiment of the DOE: the nine printing programs led to samples with substantially identical shape and volume. They all exhibit a similar green density, about 2.05 g.cm$^{-3}$. Their only difference relies on the infill pattern, according to the value (level) given to each printing parameter (factor).

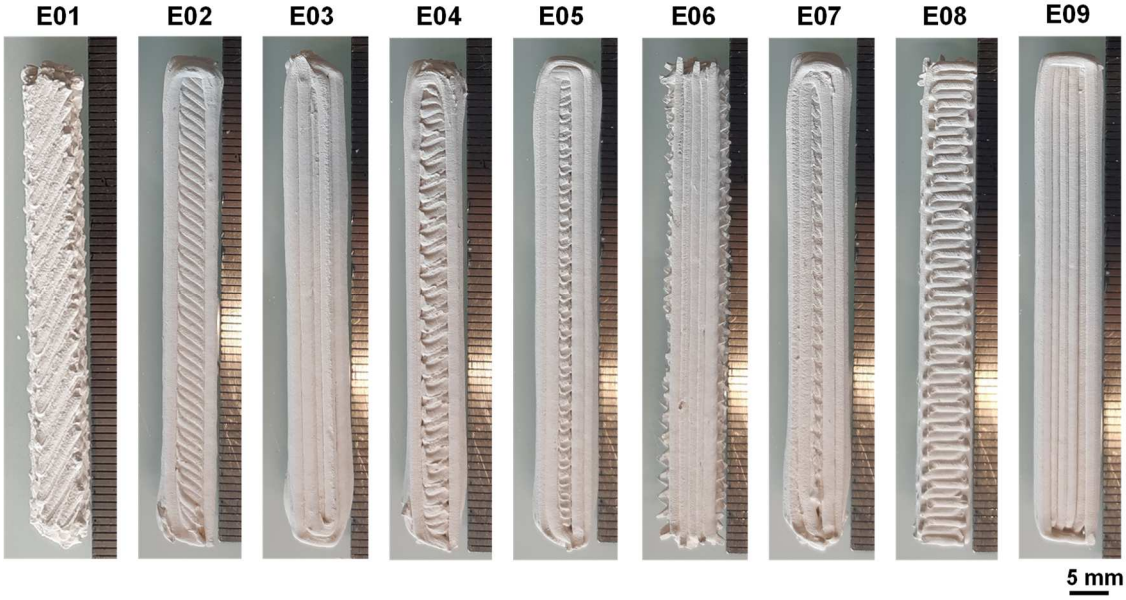


Fig. 4. Alumina green parts printed by robocasting from the nine different programs of the DOE.

### *2.3. Post-processing*

After 24 hours of drying at room temperature, all the samples of the DOE were consolidated. Debinding was performed at 500 °C (heating ramp: 0.5 °C.min$^{-1}$, dwell time: 1 hour) and sintering at 1580 °C (heating ramp: 5 °C.min$^{-1}$, dwell time: 4 hours) in a muffle furnace. These heat treatment schedules were optimized so as to densify the specimens without having an excessive grain growth (see Section 3.1.).

Post-treatment machining was carried out prior to mechanical characterizations. The surface roughness of the sintered parts was improved by polishing. In addition, chamfers were performed on the four edges of the bearing faces. These steps allow to limit the influence of

surface defects on the results of the bending tests, so that the results will only depend on the infill pattern within the parts.

*2.4. Characterization of the sintered parts*

Microstructural and mechanical characterizations were performed on at least 10 samples by experiment of the DOE, to investigate the influence of the infill pattern on the properties of the sintered parts.

Linear shrinkage was determined using geometrical measurements taken on the green (after drying) and sintered parts (before post-treatment machining steps). Measurements were taken in length, width and height. Bulk density of the sintered alumina samples was evaluated by the Archimedes method according to the ASTM B962-17 standard [22]. This method allowed to calculate relative bulk density, by using 3.91 $g.cm^{-3}$ as true alumina density value. The latter was measured with a helium pycnometer on dried P172SB alumina powder sintered at 1580 °C. The microstructure of alumina parts was observed on cross-sections with a scanning electron microscope (SEM JSM-IT300, JEOL). Cross-sections of the sintered parts of the DOE were thermally etched to reveal grain boundaries prior to SEM, in order to observe the morphology and arrangement of the grains. Average grain size was then estimated using ImageJ software. To collect representative data, image analyses were repeated at different magnifications and locations of the same sample.

A series of four-point bending tests was conducted with a universal Instron® 5969 testing system, according to the ASTM C1161-18 standard [23]. Tests were carried out with a 5 kN load cell. Load was applied perpendicular to the printing plane of the 3D specimens, at a constant speed of 0.1 $mm.min^{-1}$. The support outer span length ($L$) was 40 mm and the support inner span length ($l$) was 20 mm.

Flexural strength ($\sigma_f$) and Young's modulus ($E$) of alumina bending test parts were determined according to the following expressions:

$$\sigma_f = \frac{3F(L-l)}{2bh^2} \tag{3}$$

$$E = \frac{1}{\delta I}\left[\frac{F}{12}\left(\frac{L-l}{2}\right)^3 - \frac{3}{64}FL^2\left(\frac{L-l}{2}\right)\right] \tag{4}$$

where $F$ is the load (or force) at failure, $b$ and $h$ are respectively the width and height of the test sample, $\delta$ is the transverse displacement of the upper supports and $I$ is the second moment of area.

Elastic properties of alumina parts were measured by a non-destructive ultrasonic impulse method. Longitudinal (WC37-5, Ultran) and transverse (SWC37-5, Ultran) transducers were

placed in an acoustic contact with alumina test samples for transmitting and receiving ultrasonic waves at 5 MHz. This method completes the data obtained from bending tests by evaluating Young's modulus $E$ and other elastic properties, namely the shear modulus $G$ and the Poisson's ratio $\nu$. The elastic parameters were determined according to the following expressions:

$$E = \rho \frac{3\mathrm{v}_p^2 - 4\mathrm{v}_s^2}{\left(\frac{\mathrm{v}_p}{\mathrm{v}_s}\right)^2 - 1} \tag{5}$$

$$G = \rho \times \mathrm{v}_s^2 \tag{6}$$

$$\nu = \frac{E}{2G} - 1 = \frac{\mathrm{v}_p^2 - 2\mathrm{v}_s^2}{2\left(\mathrm{v}_p^2 - \mathrm{v}_s^2\right)} \tag{7}$$

where $\rho$ is the bulk density of the material; $\mathrm{v}_p$ and $\mathrm{v}_s$ are the velocities of longitudinal P-waves and transverse S-waves, respectively. These velocities were calculated from their wavelength and the thickness of the test sample.

## 3. Results and discussion

### *3.1. Microstructural characteristics of alumina sintered parts*

After sintering, the microstructure of the bending test parts was analysed by SEM. Little porosity is noticed between the grains, as shown in Fig. 5.a. However, this type of porosity is rather inherent to heat treatment than dependent on the infill pattern of the printed parts, since it only concerns the microscopic scale. After image analysis, similar grain size distribution was observed, regardless of the printing program, which is consistent as all the samples of the DOE underwent the same heat treatments schedules. According to Fig. 5.b, average grain size is estimated at 3.7 µm, without excessive grain growth.

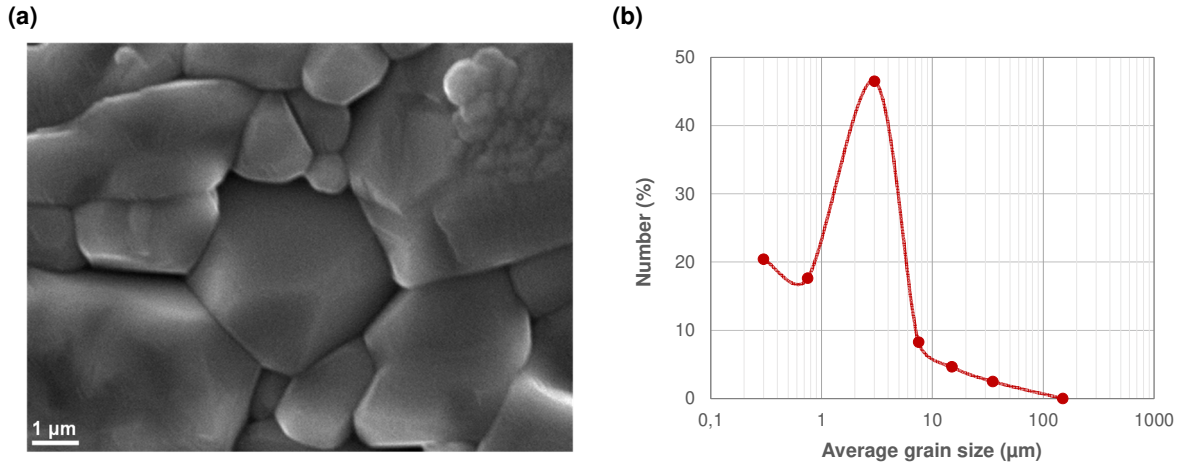


Fig. 5. Microstructure of the printed alumina parts, after sintering at 1580 °C: (a) SEM micrograph showing the morphology and arrangement of the grains and (b) average grain size distribution in number.

Alumina sintered parts exhibited an average linear shrinkage of the same order in the X, Y and Z directions of printing. Shrinkage equals to 16.7 ± 1.1% for all the samples of the DOE and remains similar from one experiment to another, since the overall results are approximately between 16 and 18% (see Fig. 6.a). This value agrees those found in the literature for alumina parts printed by robocasting [13].

Considering measurement uncertainties shown in Fig. 6.b, the samples of the DOE have a relative density of 93.1 ± 1.2% (which corresponds to an apparent density of 3.70 g.cm$^{-3}$). This value is comparable to those reported previously for robocast alumina in the literature [12,13].

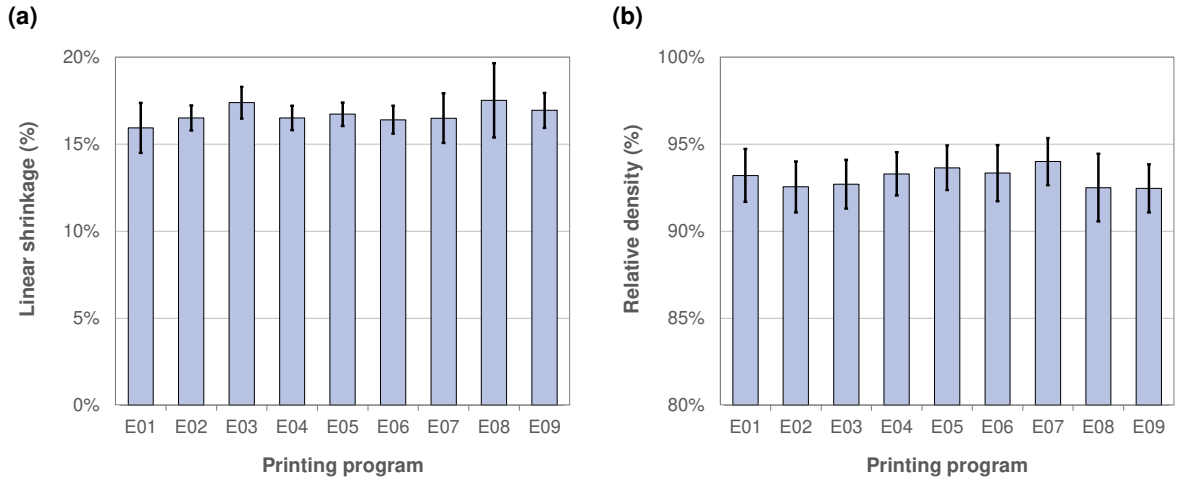


Fig. 6. Evolution of the (a) linear shrinkage and (b) relative density of the sintered alumina parts of the DOE, depending on their infill pattern.

At a macroscopic scale, open (1.9%) and closed (5.0%) porosities do not seem to change with the infill pattern as their values are similar from one printing program to another.

However, filament deposition path appears to influence the organization of closed porosity at the mesoscale within the material, as shown in Fig. 7. The samples' cross-section micrographs highlight different scenarios, in terms of location, size, shape and number of pores.

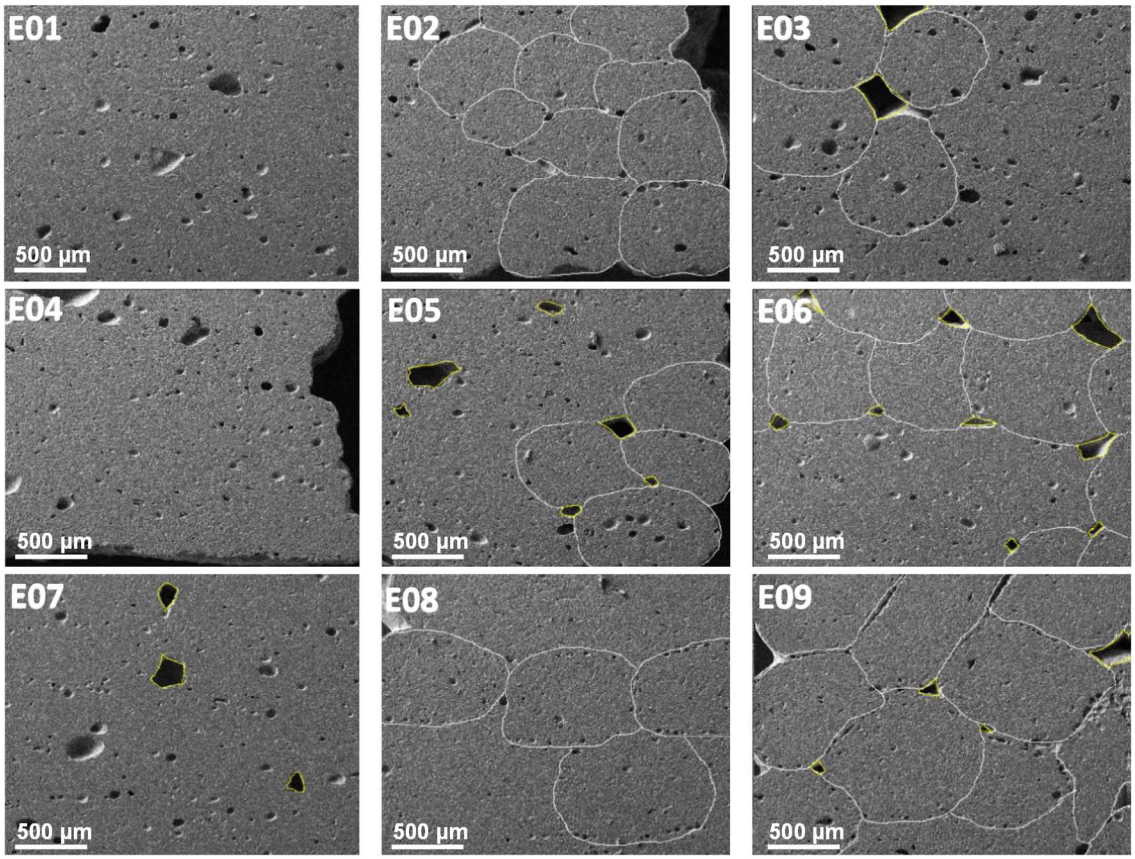


Fig. 7. SEM micrographs of the cross-section of the sintered alumina parts of the DOE, printed by robocasting. Visible filaments are circled in white and pores in-between are in yellow.

Alumina parts made from programs E01, E04 and E07 (layer thickness of 0.5 mm) look denser than other specimens, as the filament boundaries are not visible. When layer thickness increases, pores appear around the extruded filaments (see samples E02, E06, E08 and E09 in Fig. 7) which allows to distinguish their outlines.

According to Fig. 7, closed porosity can be classified into three categories, depending on its location within the parts. In ascending order of size, this concerns pores (i) between alumina grains, (ii) within the filaments (see samples E03 and E05) because of air bubbles in the paste during extrusion and (iii) between adjacent filaments, where voids have shapes similar to those described by Serdeczny *et al.* [17]. To avoid the presence of pores within the filaments, potential strategies involve incorporating a defoaming step or preventing the formation of air bubbles in the reservoir. This could be achieved by implementing a vacuum pump system at the nozzle inlet or by pre-extruding the paste through a grid before filling it into the barrel.

Nevertheless, SEM observations cannot be representative of the whole parts as it gives information in a single plane of space. Indeed, closed porosity is not distributed in an isotropic manner within the material due to the texturing imposed by the orientation of the filaments. X-ray tomography could be interesting to visualize porosity in the 3D structures.

In any case, it can be considered that pores located between the grains and within the filaments are constant parameters, not varying with the printing strategy. Instead, they depend on the paste itself (such as powder granulometry and formation of air bubbles in the reservoir) as well as sintering conditions. On the contrary, the pore category most likely to vary with the infill pattern is that located between two adjacent filaments. Indeed, the shape and/or the size of these macropores (in the order of a hundred microns) mainly depend on the printing strategy, as well as on the filament diameter. The printing of dense ceramic parts from extruded filaments involves the creation of micro- and macro-defects (*e.g.* pores, grain boundaries, etc.) [24]. The impact of these microstructural defects on the mechanical properties of brittle ceramic materials has been yet validated by several theoretical failure analyses, such as Inglis' [25], Griffith's [26] or Irwin's [27]. For instance, Griffith's experiments showed that the flexural strength $\sigma_f$ is proportional to the inverse of the square root of the critical size of the defect, such as:

$$\sigma_f \sqrt{a} \approx C \tag{8}$$

with $a$ the defect length and $C$ a constant.

Hence, the macropore distribution in the bulk of sintered parts is likely to be a determining factor for the failure behaviour (or flexural strength) and the creation of preferential crack propagation paths.

### *3.2. Mechanical properties of alumina sintered parts*

Flexural strength and elastic properties of sintered alumina parts were assessed by four-point bending test and ultrasonic impulse method (Fig. 8).

Considering the entire DOE, a similar evolution of flexural strength, Young's and shear moduli is noticed from one printing program to another. The best mechanical properties are obtained for E05 samples ($\sigma_f$ = 140 MPa, $E$ = 355 GPa, $G$ = 145 GPa) and the worst ones for E08 samples ($\sigma_f$ = 60 MPa, $E$ = 178 GPa, $G$ = 76 GPa). E05 samples exhibit elastic properties in agreement with the theoretical values of alumina ($E$ between 300 and 400 GPa, $G$ between 120 and 170 GPa). Even if flexural strength is much lower than expected (usually between 200 and 400 MPa for alumina), it is comparable to values reported in similar work in the literature [28]. For instance, Rueschoff *et al.* [16] obtained from 134 to 157 MPa (98% relative density) and Baltazar *et al.* [13] reported 170 MPa (95% relative density).

Considering the uncertainties, the differences observed between the best (E05) and the worst (E08) samples are much larger than the measurement noise (Fig. 8.a, b, c). However, all these samples were obtained from the same paste and the same heat treatments, which

gave them similar microstructural characteristics at the micro- (grain size) and macro- (shrinkage, relative density) scales. Therefore, it is assumed that the variations in mechanical properties are only due to the infill pattern of alumina parts. According to Fig. 8.b, both characterization methods led to similar Young's modulus values, which confirms the reliability of the results.

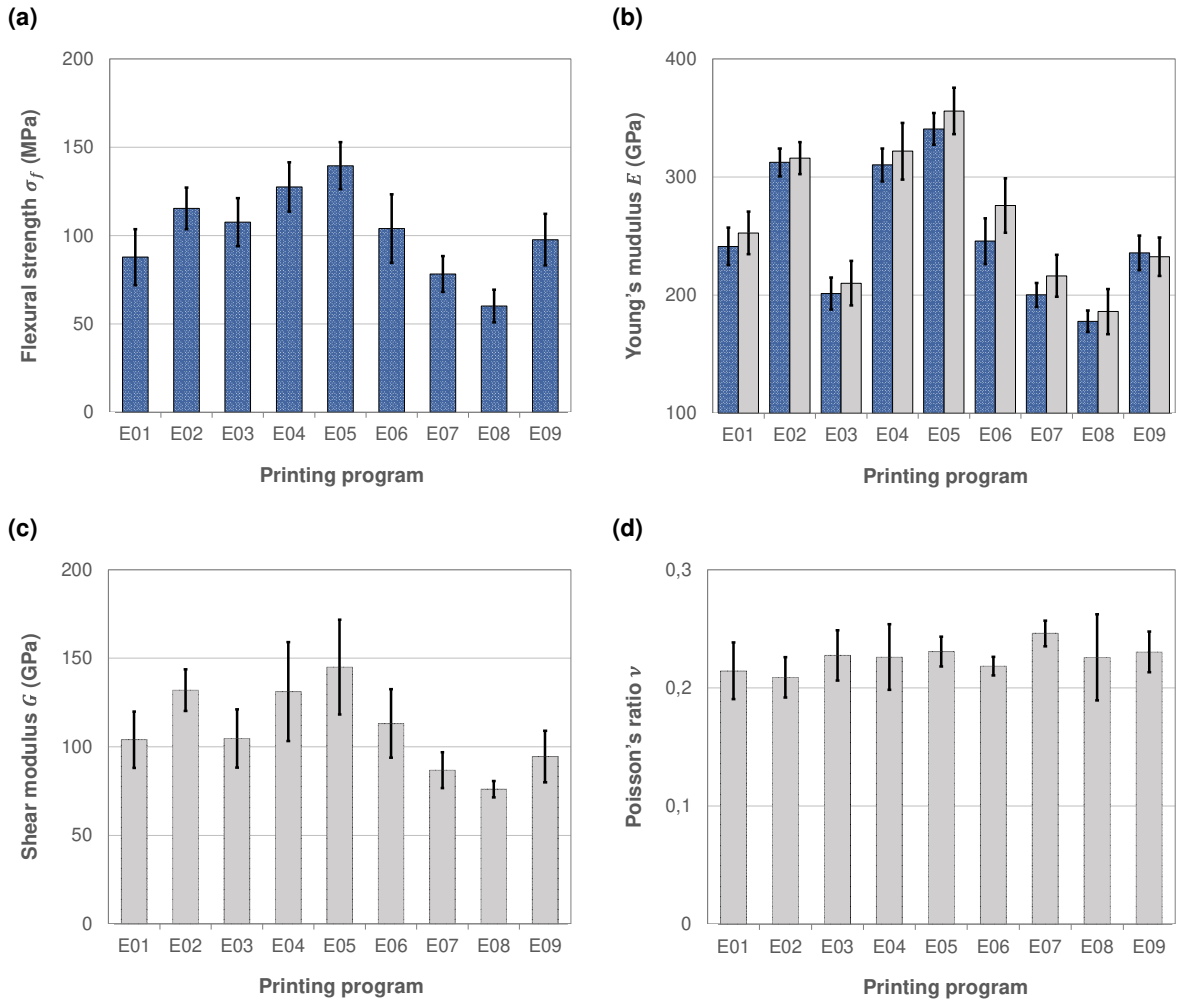


Fig. 8. Average flexural strength ($\sigma_f$) and elastic properties ($E$, $G$, $\nu$) of sintered alumina parts of the DOE, depending on their infill pattern. Histograms are coloured in dark blue when obtained from four-point bending tests and in grey when obtained from the ultrasonic impulse method.

Unlike other mechanical properties, Poisson's ratio remains constant for the overall samples of the DOE (Fig. 8.d), which is consistent given the previous results. Indeed, $\nu$ is a function of a ratio between Young's and shear moduli (see Eq. 7), the latter remaining constant (with uncertainties) since $E$ and $G$ evolve in the same way from one printing program to another. Poisson's ratio is 0.22 ± 0.02, which is comparable to data reported in the literature where $\nu$ ranges from 0.18 to 0.25, depending on the porosity of the material [29].

*3.3. Optimum printing parameters*

According to the results discussed in Section 3.2., the infill pattern of alumina specimens influences their mechanical properties, due to the internal texturing linked to different printing strategies. Taguchi design analysis was carried out to find the optimal filament deposition paths to improve the mechanical properties of sintered parts. Fig. 9 shows the main effects plots for both flexural strength and Young's modulus.

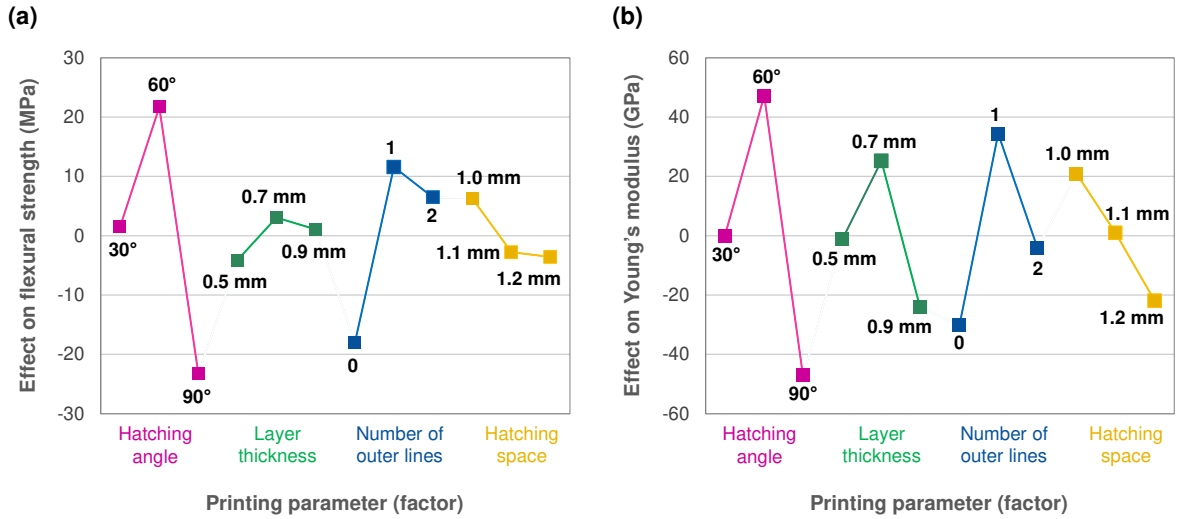


Fig. 9. Results of Taguchi design analysis, with the main effects plots for (a) flexural strength $\sigma_f$ and (b) Young's modulus $E$ obtained from ultrasonic impulse method.

Taguchi design analysis indicates similar patterns regarding the effect of each factor on both responses, namely $\sigma_f$ and $E$. This makes sense as Fig. 8 shows that they evolve in the same way from one printing program to another.

According to Fig. 9, hatching angle seems to be the most influential factor among those studied. While an optimum is observed for a hatching angle of 60°, the orientation of the filaments at 30° or 90° is likely to damage the mechanical properties. Indeed, poor adhesion of adjacent filaments may lead to more or less significant crack propagation paths, given the pores created by the fast elastic recovery of the paste after printing.

The optimum for the second factor of the DOE is a layer thickness of 70% the nozzle diameter, which agrees recommendations reported in the literature [30]. If the layers are too much (or not enough) crushed, stress (or macroporosity between the filaments) are likely to appear (see Fig. 7).

One outer line is a good compromise. It allows to smooth the outer walls of the 3D structure and to reduce open porosity close to the surface, without generating stresses likely to cause bending of the parts during the drying or sintering steps.

Printing with a hatching space of 1.0 mm is the best option among the values assessed in the DOE. Indeed, the higher the hatching space compared to nozzle diameter, to more likely it is to create porosity (despite compensation with the overflow parameter $o\mathcal{F}$).

The optimal infill pattern is a hatching angle of 60°, a layer thickness of 0.7 mm (corresponding to 70% of the nozzle diameter), 1 outer line and a hatching space of 1.0 mm. Optimal printing conditions are close to those used to manufacture E05 samples (2 outer lines instead of 1), which corresponds to the parts with the best mechanical properties, as expected. Also, the worst combination of printing parameters is close to that of E08 samples, which shows the weakest mechanical properties.

This study thus allowed to highlight the influence of the filament deposition path on the final properties of alumina sintered parts. According to Fig. 9.a, printing a part with the optimal set of parameters would increase flexural strength of 5 MPa compared to E05 samples (for which $\sigma_f$ is 140 MPa, with 2 outer lines instead of 1). Therefore, the flexural strength values obtained in this work are still lower than theoretical values of dense alumina. It is probably due to residual porosity within sintered samples, close to 7% (about 93% relative density).

### *3.4. Linking mechanical properties to the porosity generated during robocasting*

In the literature, studies regarding the mechanical behaviour of porous materials led to the development of empirical or semi-empirical models [31]. For instance, in 1953, Duckworth [32] reported that the flexural strength $\sigma_f$ of ceramic materials exponentially decreases with the porosity volume $P$, as follows:

$$\sigma_f = \sigma_0 e^{-bP} \tag{9}$$

where $\sigma_0$ is the flexural strength of the fully dense material (0% porosity) and $b$ an empirical value depending on the material. For alumina, $b$ equals 4 [33,34]. In the present work, $P$ is about 7% for the overall parts printed by robocasting (see Section 3.1.). Eq. 9 thus enables to estimate the maximum $\sigma_f$ at 150 MPa for this DOE.

Phani *et al.* [35] reported that Young's modulus of porous brittle materials is likely to evolve with porosity according to a power law, such as:

$$E = E_0(1 - aP)^n \tag{10}$$

where $E$ and $E_0$ refer to Young's modulus when porosity equals $P$ and 0%, respectively. $a$ is a constant linked to the particle stacking and $n$ depends on both grain morphology and shape of the pores [31,35,36]. Some studies have empirically shown consistent results for alumina when

$a$ is 1 and $n$ is 2.14 [35,37]. Using these values and regarding the overall specimens of the present work (7% porosity), Eq. 10 leads to a Young's modulus of 346 GPa.

Hence, Eq. 9 and Eq. 10 provide estimates of $\sigma_f$ and $E$ in agreement with the experimental results given in Fig. 8, especially for E05 samples. According to their respective models, the decrease in Young's modulus is less significant than that of flexural strength [38]. This explains why Young's moduli of E02, E04 and E05 samples (see Fig. 8.b) are included in the interval of the theoretical data for alumina, contrary to flexural strength.

Since all the samples of the DOE have similar total porosity at the macroscale, all should have similar mechanical properties. Nevertheless, a large gap was noticed between the mechanical properties of E05 and E08 samples, both having a similar porosity ratio (7%); this highlights the limits of existing analytic models to predict the mechanical behaviour of porous materials. The printing strategy is likely to generate pores between the extruded filaments and to influence their size, shape and location in the 3D part. According to Griffith's work [26], the distribution and the shape of the macropores (size in the order of a hundred microns, see Fig. 7) then affect the failure behaviour (or flexural strength) by initiating stress concentration and preferential crack propagation paths.

To decrease the size of pores and the volume of porosity in robocast parts, one of the solutions is to improve the adhesion of adjacent filaments: the higher the applied shear rate, the more fluid the paste – up to a certain shear rate, for which the viscosity is then constant. For instance, using a lower nozzle diameter could reduce paste viscosity as well as the volume of pores between the extruded filaments. All of this requires nonetheless a trade-off between achieving higher relative density (hence, better mechanical properties) and dealing with possible issues of manufacturing time, nozzle clogging, print resolution or shape fidelity.

## 4. Conclusions

An aqueous 49 vol% alumina paste, entirely based on eco-friendly additives, was successfully used to print prismatic bending test parts by robocasting. Taguchi design analysis allowed to study the influence of the filament deposition path on both microstructural and mechanical properties of sintered alumina parts. The overall samples of the DOE exhibited similar microstructural properties at the macroscale, with 93% relative density. The specific macropore distribution linked to the printing strategy leads to preferential crack propagation paths and deteriorate the strength of sintered materials. Then, a significant change in the mechanical properties of the samples was noticed in relation with the filament deposition path, depending on the infill pattern of the robocast specimens.

The present paper provides a methodology to maximize the mechanical properties under given conditions, as well as a better understanding of why and how the printing parameters influence them – a novel contribution previously lacking in the literature.

The mechanical performances have been effectively doubled between the worst and best configurations of the design of experiment. The optimal set of printing parameters was found to be a hatching angle of 60°, a layer thickness of 70% the nozzle diameter, 1 outer line and 1.0 mm of hatching space. Samples printed under optimal conditions achieved elastic properties in agreement with the literature for alumina, with a Young's modulus of 355 GPa, a shear modulus of 145 GPa and a Poisson's ratio of 0.23. Flexural strength did not exceed 140 MPa, due to its exponential decrease as a function of the porosity ratio. However, this result is comparable to some reported in the literature, considering that this study originated from an eco-friendly paste rather than a classical formulation based on petrochemical additives.

As an improvement, it would be interesting to develop a model closer to reality by considering closed pores (in terms of location, amount, size and shape) instead of a single average porosity value. For instance, X-ray tomography analyses could be coupled with a computational fluid dynamics (CFD) method, in order to clarify the link between paste rheology, infill orientation of the filaments, pore size distribution and properties of the 3D-printed parts. Numerical simulation might help to predict the key role of closed pores on sample deformation and failure. Such an approach would pave the way to enhance the mechanical properties of dense parts, by providing a universal set of optimal printing parameters and/or robocasting conditions (*e.g.* applied shear rate, nozzle diameter, etc.), regardless of the paste formulation and the 3D structure to be printed.

Two possibilities emerge in order to improve the strength of robocast materials: (i) reduce the size of macropores and control their shape, as they are stress concentration factors, by exploiting the adhesion between adjacent filaments (rheology of the paste) and/or by decreasing the volume of the voids located in-between (nozzle diameter), (ii) control the pore distribution in the solid with the printing strategy, so as to limit preferential crack propagation paths. Ultimately, solid parts with a gradient in mechanical properties could be made by robocasting, by only controlling the key parameter of closed pores through different filament deposition paths.

**Declaration of competing interest**

The authors declare that they have no known competing financial interests or personal relationships that could have appeared to influence the work reported in this paper.

**Acknowledgements**

The authors would like to sincerely thank Philippe Michaud and Nicolas Tessier-Doyen for their help and advice regarding the mechanical characterizations described in this paper.

## References


[1] J. Cesarano, A Review of Robocasting Technology, MRS Proc. 542 (1998) 133. https://doi.org/10.1557/PROC-542-133.

[2] J. Cesarano, P. Calvert, Freeforming objects with low-binder slurry, U.S. Patent 6027326, 2000.

[3] A. Zocca, P. Colombo, C.M. Gomes, J. Günster, Additive Manufacturing of Ceramics: Issues, Potentialities, and Opportunities, J. Am. Ceram. Soc. 98 (2015) 1983–2001. https://doi.org/10.1111/jace.13700.

[4] E. Udofia, W. Zhou, Microextrusion Based 3D Printing - A Review, Austin, TX, 2018.

[5] E. Feilden, E.G.-T. Blanca, F. Giuliani, E. Saiz, L. Vandeperre, Robocasting of structural ceramic parts with hydrogel inks, J. Eur. Ceram. Soc. 36 (2016) 2525–2533. https://doi.org/10.1016/j.jeurceramsoc.2016.03.001.

[6] A. M'Barki, L. Bocquet, A. Stevenson, Linking Rheology and Printability for Dense and Strong Ceramics by Direct Ink Writing, Sci. Rep. 7 (2017) 6017. https://doi.org/10.1038/s41598-017-06115-0.

[7] N. Paxton, W. Smolan, T. Böck, F. Melchels, J. Groll, T. Jungst, Proposal to assess printability of bioinks for extrusion-based bioprinting and evaluation of rheological properties governing bioprintability, Biofabrication. 9 (2017) 044107. https://doi.org/10.1088/1758-5090/aa8dd8.

[8] S. Lamnini, H. Elsayed, Y. Lakhdar, F. Baino, F. Smeacetto, E. Bernardo, Robocasting of advanced ceramics: ink optimization and protocol to predict the printing parameters - A review, Heliyon. 8 (2022) e10651. https://doi.org/10.1016/j.heliyon.2022.e10651.

[9] Z. Chen, Z. Li, J. Li, C. Liu, C. Lao, Y. Fu, C. Liu, Y. Li, P. Wang, Y. He, 3D printing of ceramics: A review, J. Eur. Ceram. Soc. 39 (2019) 661–687. https://doi.org/10.1016/j.jeurceramsoc.2018.11.013.

[10] T. Schlordt, S. Schwanke, F. Keppner, T. Fey, N. Travitzky, P. Greil, Robocasting of alumina hollow filament lattice structures, J. Eur. Ceram. Soc. 33 (2013) 3243–3248. https://doi.org/10.1016/j.jeurceramsoc.2013.06.001.

[11] P. Miranda, A. Pajares, E. Saiz, A.P. Tomsia, F. Guiberteau, Mechanical properties of calcium phosphate scaffolds fabricated by robocasting, J. Biomed. Mater. Res. 85A (2008) 218–227. https://doi.org/10.1002/jbm.a.31587.

[12] H.B. Denham, J. Cesarano, B.H. King, P. Calvert, Mechanical behavior of robocast alumina, 1998. https://doi.org/10.2172/291158.

[13] J. Baltazar, P.M.C. Torres, J. Dias-de-Oliveira, J. Pinho-da-Cruz, S. Gouveia, S. Olhero, Influence of filament patterning in structural properties of dense alumina ceramics printed by robocasting, J. Manuf. Process. 68 (2021) 569–582. https://doi.org/10.1016/j.jmapro.2021.05.043.

[14] S.M. Olhero, P.M.C. Torres, J. Mesquita-Guimarães, J. Baltazar, J. Pinho-da-Cruz, S. Gouveia, Conventional versus additive manufacturing in the structural performance of dense alumina-zirconia ceramics: 20 years of research, challenges and future perspectives, J. Manuf. Process. 77 (2022) 838–879. https://doi.org/10.1016/j.jmapro.2022.02.041.

[15] M. Maillard, J. Chevalier, L. Gremillard, G.P. Baeza, E.-J. Courtial, S. Marion, V. Garnier, Optimization of mechanical properties of robocast alumina parts through control of the paste rheology, J. Eur. Ceram. Soc. 43 (2023) 2805–2817. https://doi.org/10.1016/j.jeurceramsoc.2022.12.008.

[16] L. Rueschhoff, W. Costakis, M. Michie, J. Youngblood, R. Trice, Additive Manufacturing of Dense Ceramic Parts via Direct Ink Writing of Aqueous Alumina Suspensions, Int. J. Appl. Ceram. Technol. 13 (2016) 821–830. https://doi.org/10.1111/ijac.12557.

[17] M.P. Serdeczny, R. Comminal, D.B. Pedersen, J. Spangenberg, Numerical simulations of the mesostructure formation in material extrusion additive manufacturing, Addit. Manuf. 28 (2019) 419–429. https://doi.org/10.1016/j.addma.2019.05.024.

[18] M.G.A. Vieira, M.A. da Silva, L.O. dos Santos, M.M. Beppu, Natural-based plasticizers and biopolymer films: A review, Eur. Polym. J. 47 (2011) 254–263. https://doi.org/10.1016/j.eurpolymj.2010.12.011.
[19] A. Aimable, T. Chartier, Organic Additives in Ceramic Processing, in: Encycl. Mater. Tech. Ceram. Glas., Elsevier, Oxford, 2020: pp. 103–111. https://doi.org/10.1016/B978-0-12-803581-8.11768-0.
[20] D. Gourdonnaud, Micro-extrusion de pâtes céramiques innovantes respectueuses de l'environnement : relation entre formulation, imprimabilité, stratégie de dépôt et propriétés mécaniques des pièces frittées, PhD thesis, University of Limoges, 2022. https://www.theses.fr/2022LIMO0135 (accessed February 8, 2023).
[21] W.H. Herschel, R. Bulkley, Konsistenzmessungen von Gummi-Benzollösungen, Kolloid-Z. 39 (1926) 291–300. https://doi.org/10.1007/BF01432034.
[22] ASTM International, ASTM B962-17 - Test Methods for Density of Compacted or Sintered Powder Metallurgy (PM) Products Using Archimedes Principle, ASTM International, 2017. https://doi.org/10.1520/B0962-17.
[23] ASTM International, ASTM C1161-18 - Standard Test Method for Flexural Strength of Advanced Ceramics at Ambient Temperature, ASTM International, 2018.
[24] N. Tessier-Doyen, Étude expérimentale et numérique du comportement thermomécanique de matériaux réfractaires modèles, PhD thesis, University of Limoges, 2003.
[25] C.E. Inglis, Stresses in a plate due to the presence of cracks and sharp corners, Proc Inst Nav. Arch. 55 (1913) 219–241.
[26] A.A. Griffith, The Phenomena of Rupture and Flow in Solids, Phil Trans Roy Soc Lond. 221 (1920) 163–198.
[27] G.R. Irwin, Analysis of Stresses and Strains Near the End of a Crack Traversing a Plate, J. Appl. Mech. 24 (1957) 361–364.
[28] E. Peng, D. Zhang, J. Ding, Ceramic Robocasting: Recent Achievements, Potential, and Future Developments, Adv. Mater. 30 (2018) 1802404. https://doi.org/10.1002/adma.201802404.
[29] M. Asmani, C. Kermel, A. Leriche, M. Ourak, Influence of porosity on Young's modulus and Poisson's ratio in alumina ceramics, J. Eur. Ceram. Soc. 21 (2001) 1081–1086. https://doi.org/10.1016/S0955-2219(00)00314-9.
[30] S. Tang, L. Yang, G. Li, X. Liu, Z. Fan, 3D printing of highly-loaded slurries via layered extrusion forming: Parameters optimization and control, Addit. Manuf. 28 (2019) 546–553. https://doi.org/10.1016/j.addma.2019.05.034.
[31] J.A. Choren, S.M. Heinrich, M.B. Silver-Thorn, Young's modulus and volume porosity relationships for additive manufacturing applications, J. Mater. Sci. 48 (2013) 5103–5112. https://doi.org/10.1007/s10853-013-7237-5.
[32] W. Duckworth, Discussion of Ryshkewitch paper, J. Am. Ceram. Soc. 36 (1953) 68–69.
[33] F.P. Knudsen, Dependence of Mechanical Strength of Brittle Polycrystalline Specimens on Porosity and Grain Size, J. Am. Ceram. Soc. 42 (1959) 376–387. https://doi.org/10.1111/j.1151-2916.1959.tb13596.x.
[34] R.A. Dorey, J.A. Yeomans, P.A. Smith, Effect of pore clustering on the mechanical properties of ceramics, J. Eur. Ceram. Soc. 22 (2002) 403–409. https://doi.org/10.1016/S0955-2219(01)00303-X.
[35] K.K. Phani, S.K. Niyogi, Young's modulus of porous brittle solids, J. Mater. Sci. 22 (1987) 257–263. https://doi.org/10.1007/BF01160581.
[36] J. Kováčik, Correlation between Young's modulus and porosity in porous materials, J. Mater. Sci. Lett. 18 (1999) 1007–1010. https://doi.org/10.1023/A:1006669914946.
[37] A.S. Wagh, R.B. Poeppel, J.P. Singh, Open pore description of mechanical properties of ceramics, J. Mater. Sci. 26 (1991) 3862–3868. https://doi.org/10.1007/BF01184983.
[38] D. Liu, B. Šavija, G.E. Smith, P.E.J. Flewitt, T. Lowe, E. Schlangen, Towards understanding the influence of porosity on mechanical and fracture behaviour of quasi-brittle materials: experiments and modelling, Int. J. Fract. 205 (2017) 57–72. https://doi.org/10.1007/s10704-017-0181-7.